The Effect of Morphology of Ternary-Phase Polypropylene/Glass Bead/Ethylene-Propylene Rubber Composites on the Toughness and Brittle-Ductile Transition

I. L. DUBNIKOVA, S. M. BEREZINA, A. V. ANTONOV

N.N. Semenov Institute of Chemical Physics, RAS, 4 Kosygin st., Moscow 119991, Russia

Received 23 July 2001; accepted 6 November 2001

ABSTRACT: Correlation between the morphology and the impact toughness was studied for ternary-phase polypropylene (PP)/glass bead (GB)/ethylene-propylene rubber (EPR) composites containing 5–40 vol % of rigid filler at a fixed volume fraction ratio EPR/GB equal to 0.33. The three following types of phase morphology were obtained: (1) separate dispersion of phases and weak GB–PP adhesion; (2) separate dispersion of phases and high GB–PP adhesion; and (3) encapsulation of GB particles by elastomer shell. Maleated PP or EPR was used for the preparation of second and third types of composites, respectively. Binary composites with either rigid or rubbery phases were prepared as model systems. Young's modulus values of composites containing GB encapsulated by a soft interlayer stay close to neat PP modulus and are located in the bounds corresponding to ternary systems with phase-separate distribution and rubber-modified PP. Notched impact strength was measured by Izod and three-point bending tests. Systems with the phase-separate distribution both with weak and with high adhesion exhibit quasi-brittle fracture. The encapsulation of GB particles by elastomer results in significant improvement of the toughness. An increase in core-shell inclusion fraction leads to intense matrix yielding within a specimen bulk and brittle–ductile transition similar to the rubber-toughened PP. A criterion of brittle–ductile transition was proposed on the basis of load-time curve analysis, which is an accumulation of critical plastic deformation on a crack initiation stage. The stress of start of local failure microprocesses at the inclusion–matrix boundary was found to play the dominating role in energy-dissipating mechanisms. The lowering of the stress at which a local matrix yielding starts at elastomer shell–PP interface compared to the stress of GB debonding is a main source of intensive energy adsorption at the initiation stage in the system with encapsulated GB. The optimal stiffness–toughness balance can be obtained by coating the rigid particles with an elastomer shell. J Appl Polym Sci 85: 1911–1928, 2002

Key words: polypropylene composites; phase morphology; impact toughness; fracture mechanism; brittle–ductile transition

INTRODUCTION

Isotactic polypropylene (PP) is characterized by a good moldability, low-density, high-softening point and is widely used in a variety of applications, but its toughness is not sufficient for the application as engineering plastic. As known semicrystalline polymers [PP, high-density polyethylene (HDPE), poly(amide-6) (PA-6), bisphenol-A polycarbonate (PC)] exhibit a ductile behavior at low loading rates, a low crack propagation resistance and brittle fracture occur at impact conditions. Toughening of polymers by rubber is

Correspondence to: I. L. Dubnikova (ild@chph.ras.ru).
Contract grant sponsor: Russian Foundation of Fundamental Research; contract grant number: 01-03-32043.

Journal of Applied Polymer Science, Vol. 85, 1911–1928 (2002)

one of the most widely used methods. A strong dependence of the notched fracture behavior of rubber–polymer blends on the morphology (particle size and rubber content)[1–10] and elastomer mechanical properties[11–14] was shown. A relief of the hydrostatic tension ahead of a crack tip by rubber cavitation is accepted as a main toughening mechanism.[13–19] A number of criteria of brittle–ductile transition have been proposed: the critical interparticle distance[3–5,20,21] and the critical precrack plastic zone volume,[7,22] in particular. However, rubber toughening is accompanied by a reduction in a material modulus. To improve toughness without a dramatic loss in stiffness, a creation of ternary-phase composites containing both rubbery and rigid fillers is extensively investigated at present. Two opposite types of a phase morphology of the ternary composites can be formed, either a separate dispersion of rubbery and rigid phases or encapsulation of rigid particles by an elastomer shell and formation by the way of core–shell inclusions. Numerous studies were devoted to the problem of the morphology–impact resistance correlation in the multicomponent systems.[23–31] However, the conclusions of authors contradict one another. The effect of the ternary-phase composite morphology on the microdeformation processes and fracture mechanism is still not clearly understood.

The purpose of this work is to investigate the effect of phase morphology, inclusion volume fraction, and interfacial adhesion on the toughness and the fracture mechanisms of ternary-phase PP/glass bead (GB)/ethylene-propylene rubber (EPR) composites. To elucidate microdeformation processes accompanying ductile fracture and conditions of brittle–ductile transition, the behavior of ternary composites was compared to that of model binary systems containing either rubbery (PP/EPR) or rigid (PP/GB) inclusions.

EXPERIMENTAL

Materials

Isotactic polypropylene (PP) with a melt flow rate (MFR) of 0.38 g/10 min (190°C, 5 kg) was used as a matrix polymer ($M_w = 4.8 \times 10^5$ g/mol, $M_w/M_n = 3.7$). Surface-treated glass beads (Potters-Ballotini 5000 CP-03) containing 0.02 wt % aminosilane, with average particle diameter of about 3.5 μm (particle diameters are in the range of 1–10 μm), were used as a rigid filler. Ethylene-propylene copolymer (EPR) Dutral CO 043 (Italy) was used as a rubbery component. Composite morphology was controlled by the application of functionalized components: maleic anhydride-grafted PP (MPP) and maleic anhydride-grafted EPR (MEPR), both supplied by Exxon Chemical Co. (Deutsche EXXON CHEMICAL GmbH). MPP [Exxelor P02011; MFR = 15 g/10 min (190°C, 1.05 kg)] was used to improve the matrix–filler adhesion. MEPR [Exxelor VA1803, MFR = 3 g/10 min (230°C, 2.16 kg)] was used to promote encapsulation of rigid particles by elastomer.

Compounding

All composites were prepared by mixing the components by a one-step procedure (Brabender mixing chamber, 190°C, 60 rpm, 10 min). Thermal stabilizers, topanol (0.3 wt %) and dilauriltiodipropionate (0.5 wt %), were used. Three series of ternary composites were prepared: PP/GB/EPR, MPP/GB/EPR, and PP/GB/MEPR. Binary PP/EPR and PP/GB composites were also prepared as model systems. Volume fraction of GB was varied in the range of 5–40%. The volume fraction ratio EPR/GB was fixed and kept equal to 0.33. This value was chosen to provide 10% of GB radius for the rubbery shell thickness in the case of rigid particle encapsulation.

Specimen Preparation

The specimens for morphological and mechanical testing were prepared by compression molding. The molding procedure involves heating at 190°C for 5 min without applied pressure and then for 5 min under pressure (10 MPa). The mold was cooled to 90°C by water at a rate of 16°C/min under pressure.

Tensile Test

Tensile properties were measured at ambient temperature by using a tensile testing machine (Instron-1122) with a crosshead speed of 20 mm/min (0.67 min^{-1}). Dumbbell specimens were cut from 0.5-mm-thick molded sheets.

Impact Tests

The impact strength of notched specimens was measured at ambient temperature by Izod and three-point bending tests. Izod impact tests were carried out at 2.9 m/s on rectangular bars 80 × 10 × 4 mm with single-edge 45° V-shaped notch (tip

radius, 0.25 mm; depth, 1.5 mm). Three-point bending tests were carried out at 2.6 m/s on rectangular bars 40 × 6 × 4 mm also with a single-edge 45° V-shaped notch (tip radius, 0.25 mm; depth, 1.5 mm).

Scanning Electron Microscopy (SEM)

The composite-phase morphology and microdeformation processes during fracture were examined by scanning electron microscopy by using a JEOL JSM-35C. To elucidate the composite morphology in terms of phase distribution, the samples were cryogenically fractured and the surfaces were etched by heptane (to remove the EPR component from the surface). The failure modes and microdeformation processes were studied by analysis of the fracture surfaces and the structure of damage zones perpendicular to the crack plane on impact fractured specimens. All specimens were gold-sputtered before SEM analysis.

RESULTS AND DISCUSSION

Composite Morphology

The micrographs of etched fracture surfaces of ternary composites are shown in Figure 1. Small circular holes (~ 0.5–1 μm diameter) are imprints of EPR particles. Large dark areas are formed as GB particles are pulled out during a fracture. Microstructure of PP/GB/EPR composite [Fig. 1(a)] demonstrates a separate dispersion of the GB and EPR particles as well as debonding of GB particles caused by a weak interfacial adhesion between the GB and the PP host. In the MPP/GB/EPR system [Fig. 1(b)], the rigid and rubbery phases are also separately dispersed, but the GB particles remain attached to polymer, demonstrating a high interfacial adhesion. The effect of using a modified rubber is apparent in Figure 1(c) for the PP/GB/MEPR composite, where there is evidence of encapsulation of rigid particles by elastomer shell. The thickness of the elastomer layer formed is ~ 10–20% of the GB particle radius. However, some GB particles were found to stay nonencapsulated. In the model PP/EPR system, the rubber forms a dispersed phase with a particle size of 0.5–2 μm.

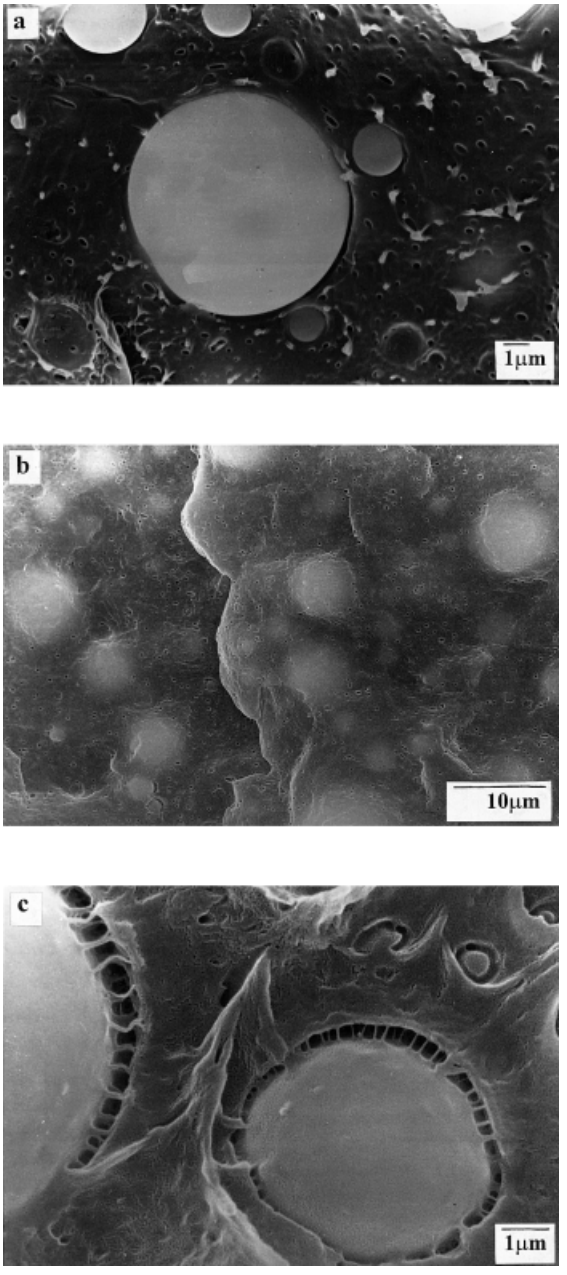

Figure 1 The SEM micrographs of cryogenically fractured and etched surfaces of the ternary composite specimens containing 10 vol % GB and 3.3 vol % EPR: (a) PP/GB/EPR, (b) MPP/GB/EPR, (c) PP/GB/MEPR.

The Effect of the Morphology and Inclusion Volume Fraction on the Young's Modulus and the Yield Stress of Ternary and Model Binary Composites at a Tensile Test

The dependencies of relative Young's modulus upon the total inclusion volume fraction $\Phi_{tot} = \Phi_{GB} + \Phi_{EPR}$ are shown in Figure 2 for ternary and model binary composites. The moduli of ternary-phase composites are seen to be located between the bounds corresponding to binary composites containing either rigid (GB) or soft (EPR) inclusions. Modulus values of ternary systems with the separate dispersion of GBs and rubber phase are higher than those of ternary system with the en-

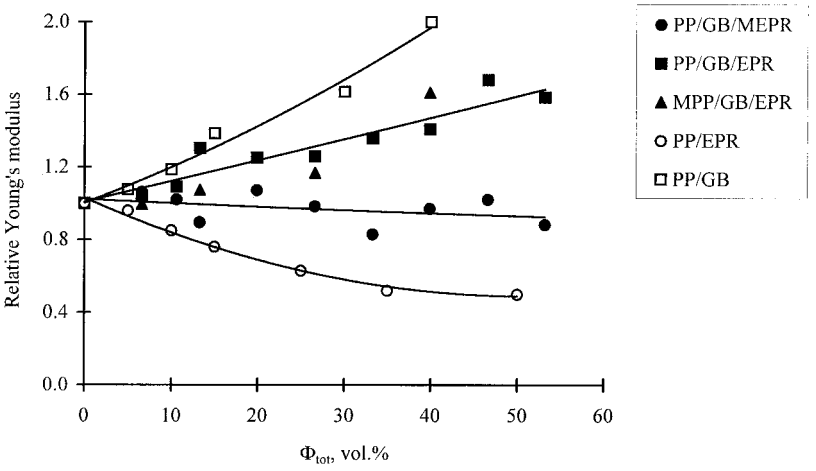

Figure 2 Relative Young's modulus as a function of the total inclusion volume fraction for ternary and model binary composites.

capsulated GB particles. The Young's modulus of the PP/GB/EPR and MPP/GB/EPR systems increases with increasing Φ_{tot} and does not depend on matrix–filler interfacial adhesion, whereas modulus values of the ternary PP/GB/MEPR system remain close to PP modulus at all Φ_{tot}. The decrease in Young's modulus of the ternary-phase composite as a result of encapsulation of rigid particles by elastomer shell was also previously found by Jancar and Dibenedetto.[23] Thus, the transfer of rubber from the bulk matrix to a shell around the rigid particle reduces the reinforcing efficiency of the filler acting similar to an increase in elastomer content. The fact that the noticeable drop of the PP/GB/MEPR modulus with Φ_{tot} was not observed is likely caused by the presence of a certain portion of nonencapsulated rigid particles (in accordance with microscopic data) and particles coated by a thin soft layer.

In Figure 3(a), the composite yield stresses at a tensile test are plotted versus a total inclusion volume fraction. An increase in inclusion content results in a decrease in yield stress for every composite. It is notable that yield stress values for both binary PP/EPR and PP/GB systems coincide. These data establish that both rubber particles and voids, formed as a result of debonding GB particles from PP (due to weak interface adhesion in the PP/GB composites), equally decrease the polymer resistance to plastic deformation. The yield stresses of the ternary systems containing both GB and EPR phases, at a corresponding total inclusion volume fraction, are practically the same as those of binary systems. The composition dependence of yield stresses obtained coincides well with that corresponding to effective loading section model. The high interfacial adhesion between the GB particles and polymer becomes apparent as a tendency to increasing yield stress of the MPP/GB/EPR composites at a high filler content.

The ternary system morphology affects most strongly the shape of σ-ε curves and the composite yield strains. Figure 4 shows the initial portions of the σ-ε curves of the ternary systems at two Φ_{tot} values. It is seen that an increase in inclusion content leads to a sharper decrease in yield strains of the MPP/GB/EPR and PP/GB/EPR composites than those of the PP/GB/MEPR system. It means that an accumulation of plastic deformations occurs more locally along the specimen length. This effect is especially emphasized for the MPP/GB/EPR system with high adhesion between GB and PP [Fig. 3(b)]. The matrix yielding starts first in a casual zone with partly debonded GB particles. Finally, a tendency to plastic flow localization results in an embrittlement of the MPP/GB/EPR composites at a lower inclusion content. The maximum stress observed on the σ-ε curves should be considered as an apparent yield stress because of a high heterogeneity of plastic deformation in MPP/GB/EPR system.

The Effect of Morphology and Inclusion Volume Fraction on the Impact Strength of Ternary and Model Binary Composites

The relative impact strengths of ternary and binary systems are shown in Figure 5 as functions of the total inclusion volume fraction. The results

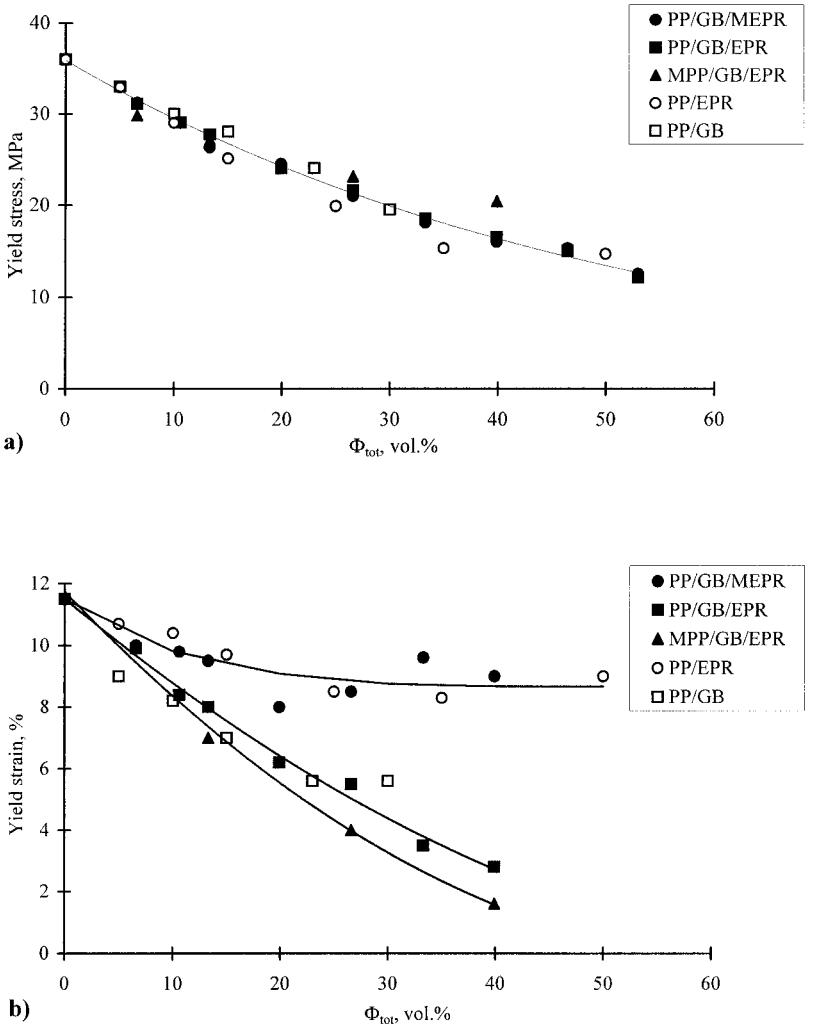

Figure 3 The yield stress (a) and yield strain (b) values as functions of the total inclusion volume fraction for ternary and model binary composites.

obtained by two impact test methods are similar. When GB and EPR are separately dispersed in PP matrix, the impact strengths of ternary composites with both weak and high interfacial adhesion are low and slightly higher than those of the binary PP/GB system. The slightly emphasized extreme dependencies of the impact strength upon the inclusion volume fraction are observed for PP/GB/EPR and MPP/GB/EPR ternary composites as well as for the binary PP/GB system. The impact strengths attain maximum values in the region of Φ_{tot} = 10–15 vol % and are equal to 2.6 and 3.4 kJ/m^2 for MPP/GB/EPR and PP/GB/EPR composites correspondingly (i.e., run up to 1.2–1.6 times compared to that of the neat PP). An increase in the adhesion between GB and PP resulted in a decrease in the toughness of the ternary-phase system. A similar effect of the interfacial adhesion on the impact strength of particulate-filled PP was previously observed by us for binary PP/GB composites.[32] In contrast to the morphology with the phase-separate dispersion, the toughness of ternary composites with the GB particles encapsulated by an elastomer shell monotonously increases with an increase in the inclusion content up to 4.5 times at Φ_{tot} = 53 vol % compared to neat PP. The toughness of the model binary PP/EPR system rises to 10 times at 25 vol % of EPR and the specimens containing the rubber modifier higher than 10 vol % were not broken completely (dotted portion of an Izod test curve). Thus, the ternary system toughness in the case of the encapsulation of rigid particles by elastomer is higher than that in the case of the phase-sep-

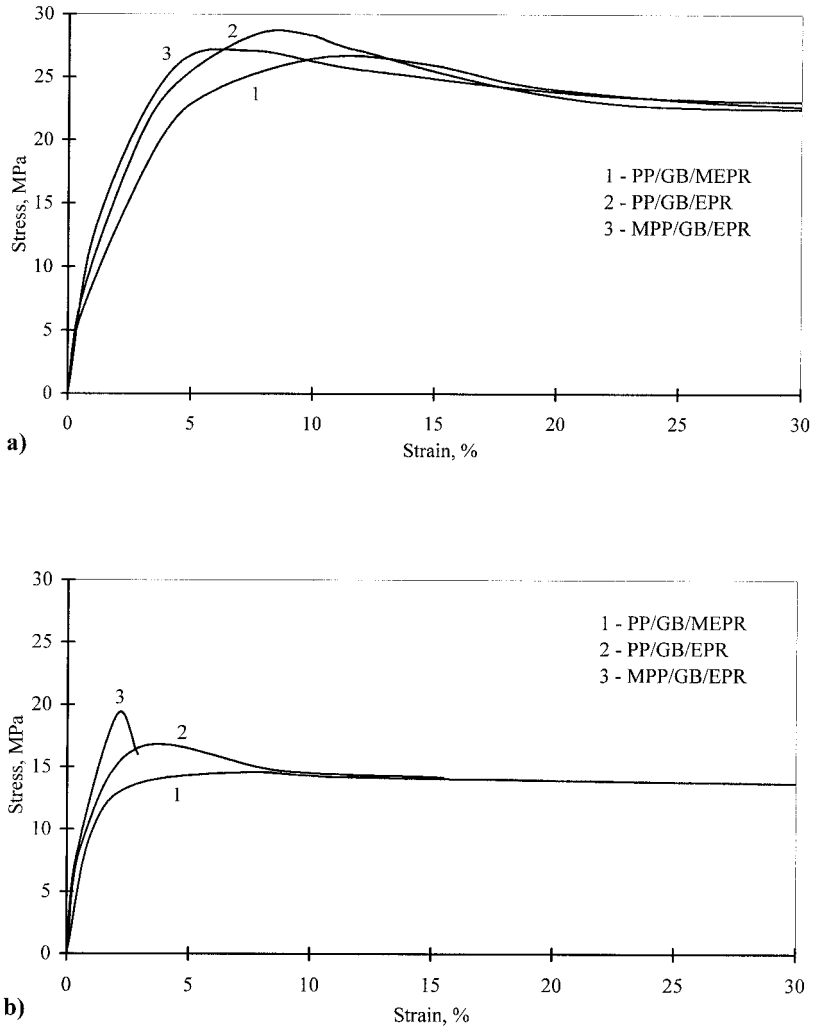

Figure 4 Initial portions of stress–strain diagrams of ternary composites with Φ_{tot} = 13 vol % (a) and Φ_{tot} = 40 vol % (b).

arate distribution, but one is lower than the model tough PP/EPR system. Data obtained show that the rubber-phase spatial disposition strongly affects the ternary system toughness.

The Fracture Behavior and Brittle–Ductile Transition

The Analysis of Load-Time Diagrams

The composite fracture behavior was examined by an analysis of the three-point bending load-time diagrams. Load-time diagrams for ternary (a–c) and binary PP/EPR (d) composites at various inclusion contents are given in Figure 6. Their shape enables us to clarify a type of composite fracture.[33,34] The fracture process may be divided into a crack initiation stage (up to force maximum on load-time diagram) and a crack propagation stage. Crack propagation is assumed to start at or just past the maximum stress. The energy adsorbed during each stage is a function of two factors: the deformation and the stress. An increase in the displacement and the energy on the crack propagation stage indicates a transformation of a fracture type from brittle to ductile. The onset of the rise in the crack propagation deformation is considered the brittle–ductile transition.[33,34] A series of fracture parameters were determined from the load-time diagrams: maximum stress (force maximum divided by the cross-sectional area behind the notch), crack initiation displacement (CID) and energy (CIE), crack propagation displacement (CPD) and energy (CPE), as well as a total fracture displacement and energy.

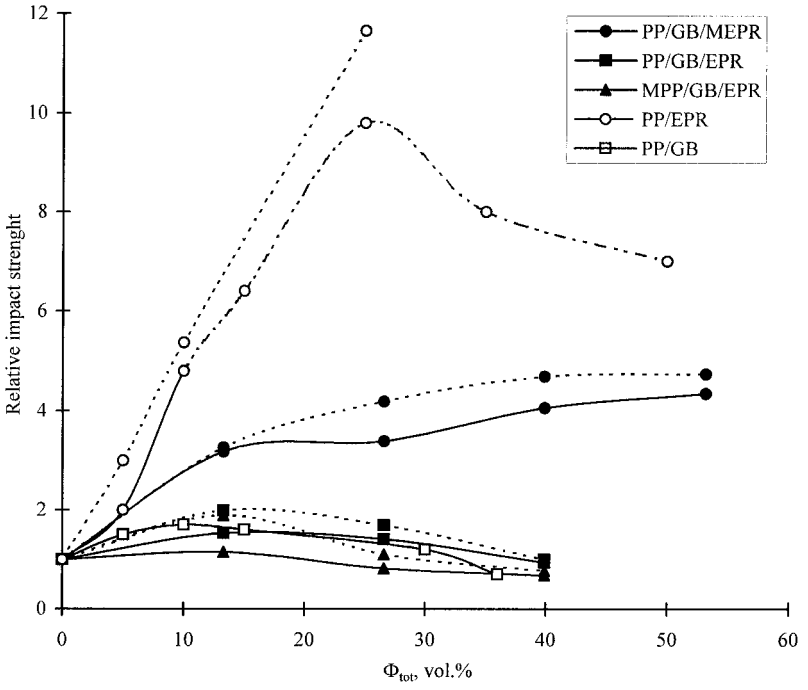

Figure 5 Relative impact strength as a function of the total inclusion volume fraction for ternary and binary composites fractured by Izod (—) and three-point bending tests (- - -).

The displacement was calculated as a product of the deformation rate and the time. The supplied energy values on each of the stages were calculated by integrating the load-displacement curve up to or behind force maximum, correspondingly.

Figure 7 shows the crack initiation, crack propagation, and fracture displacements versus the total inclusion volume fraction for the ternary composites in comparison with the model binary PP/EPR system. When the rigid and rubber phase are distributed separately, the CIDs for both ternary systems are low and exhibit a slightly emphasized maximum with respect to the total inclusion volume fraction [Fig. 7(a)]. The CPD does not rise at any Φ_{tot} [Fig. 7(b)]. Fracture type of corresponding composites can be classified as a brittle (at least on a macroscopic scale). On the other hand, in the PP/GB/MEPR system, as one can see from load-time diagrams [Fig. 6(c)], considerable inelastic deformation during the crack initiation stage precedes the crack propagation, and the CID continuously increases with increasing encapsulated GB fraction [Fig. 7(a)]. At Φ_{tot}, above 40 vol %, a sharp rise in the crack propagation displacement occurs [Fig. 7(b)] and a fracture type changes from brittle to ductile. A jump in a total fracture displacement at Φ_{tot} higher than 40 vol % [Fig. 7(c)] is directly related to raising CPD [Fig. 7(b)].

Figure 8 shows the maximum stress as a function of the total inclusion volume fraction for the ternary and PP/EPR systems. A change in a slope in maximum stress–Φ_{tot} curves is observed for every system. The maximum stresses for the PP/GB/EPR and MPP/GB/EPR systems at every inclusion content are the fracture stresses at a brittle failure mode. Positions of the maximum values on maximum stress–Φ_{tot} curves are attained at the same Φ_{tot} as maximum CID values. Maximum stresses for the PP/GB/MEPR system are higher than those of the systems with phase-separate distribution. An essential drop in a slope in the maximum stress–Φ_{tot} curve occurs in the region of the transition from brittle to ductile failure mode and past the maximum point the maximum stress transforms from the fracture stress into the yield stress. In a ductile region, a decrease in the maximum stress corresponds to a decrease in the composite yield stress with the Φ_{tot} at the tensile test [Fig. 3(a)].

Figure 9 shows crack initiation, crack propagation, and total fracture energies versus the total inclusion volume fraction. The composition dependencies of the supplied energies result from

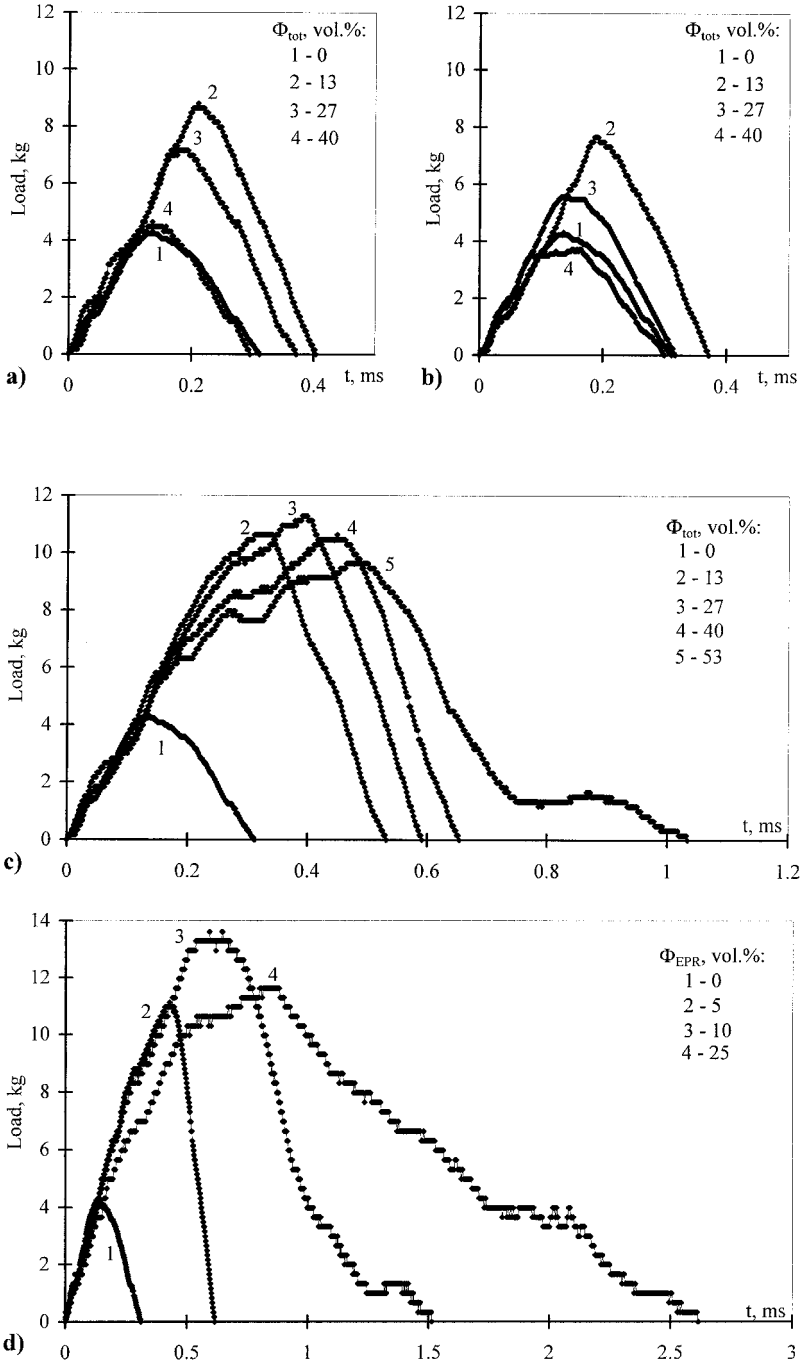

Figure 6 Load-time diagrams for ternary PP/GB/EPR (a), MPP/GB/EPR (b), PP/GB/MEPR (c), and binary PP/EPR (d) composites at various inclusion contents.

corresponding dependencies of displacements and stresses experienced during each stage. For PP/GB/EPR and MPP/GB/EPR systems, CIE [Fig. 9(a)] and CPE [Fig. 9(b)] exhibit negligible maximum with respect to inclusion fraction. The observed characters of the CIE–Φ_{tot} and the CPE–Φ_{tot} dependencies correlate with a slight extreme for corresponding displacements [Fig. 7(a,b)] and for maximum stress (Fig. 8). So, an extreme type of fracture toughness composition dependencies for both ternary systems with the phase-separate distribution [Figs. 5 and 9(c)] is clarified by the analysis performed. A distinctive feature of the PP/GB/MEPR system is a high-energy adsorption

during crack initiation stage [Fig. 9(a)]. Up to Φ_{tot} = 40 vol %, the CIE increases with an increase in encapsulated GB content. Mainly, it is a result of an increase in CID [Fig. 7(a)]. At higher inclusion fraction, the CIE decreases because a drop in the stress (Fig. 8) is stronger than an increase in the CID. The crack propagation energy rises sharply at Φ_{tot}'s higher than 40 vol % [Fig. 9(b)]. The jump of the CPE is due to a sharp increase in the CPD [Fig. 7(b)] and is predominate over a decrease in the stress. A rise in an energy adsorbed during the crack propagation stage is evidence of the transition to the ductile failure mode. At the same time, the total fracture energy increases gradually with increasing inclusion content without observable threshold on the composition dependence curve [Fig. 9(c)]. This gradual manner is caused by the competition between a rise in the CPE and a decrease in the CIE at Φ_{tot} higher than 40 vol %. The data obtained show that the crack propagation displacement is a more accurate indicator of the brittle–ductile transition compared to a total fracture energy.

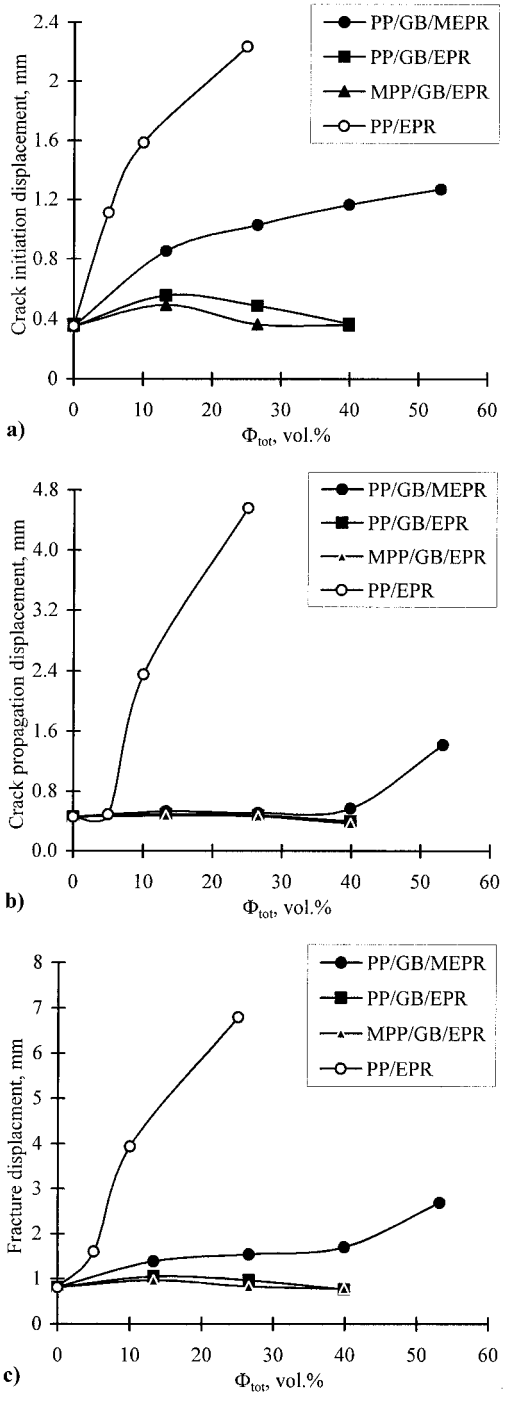

Figure 7 The crack initiation (a), crack propagation (b), and fracture displacements (c) versus the total inclusion volume fraction for ternary and PP/EPR systems.

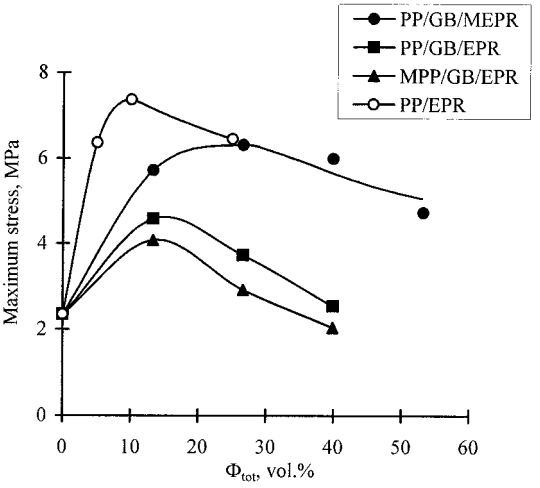

Figure 8 The maximum stress as a function of the total inclusion volume fraction for the ternary and PP/EPR systems.

The load-time diagram analysis has shown certain similarities of the fracture behavior of the system with encapsulated rigid particles and model tough PP/EPR system: (1) the crack initiation displacement increases with an increase in the inclusion fraction [Fig. 7(a)] and (2) a sharp rise in the crack propagation displacement [Fig. 7(b)] and crack propagation energy [Fig. 9(b)] takes place at a certain inclusion content. However, the corresponding rubber content in the PP/EPR system is in range of 5–10 vol %, whenever the corresponding encapsulated GB content is higher than 40 vol %. The same crack initiation displacement, leading to the effect of sharp rais-

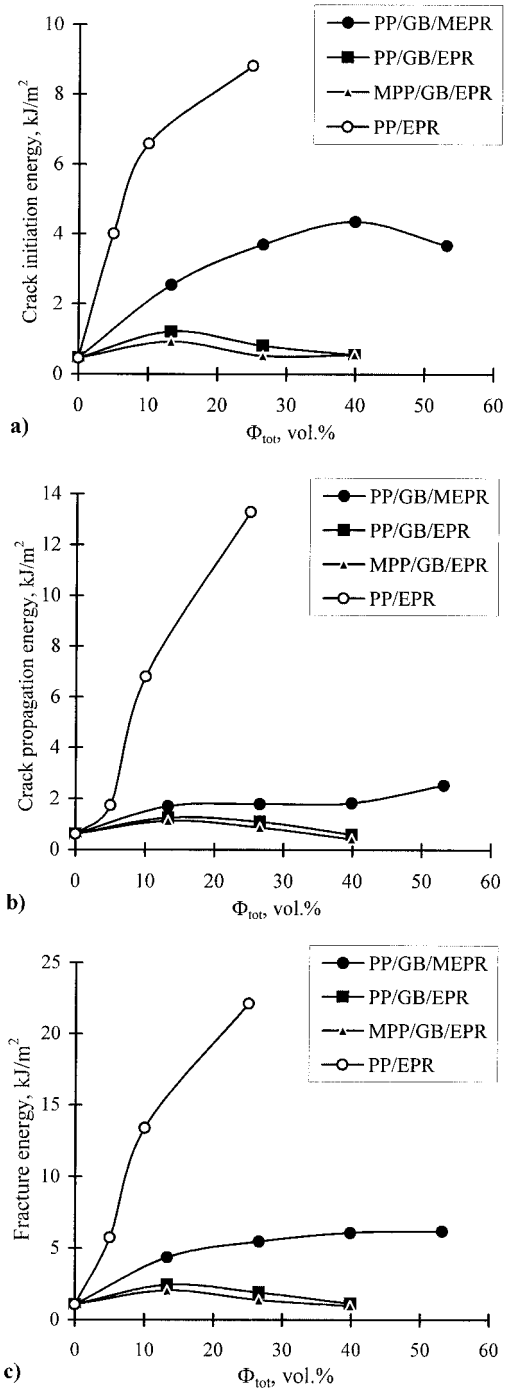

Figure 9 The crack initiation (a), crack propagation (b), and fracture energies (c) versus the total inclusion volume fraction for ternary and PP/EPR systems.

ing of the deformation on the crack propagation stage, was established for both the rubber-toughened system and ternary system with encapsulated GB (Fig. 10). On the basis of the load-time diagram analysis, it was concluded that an accumulation of the critical plastic deformation during the crack initiation stage is a criterion of a brittle-ductile transition. In the region of the ductile fracture, the maximum stresses for both PP/GB/MEPR and PP/EPR composites become close and form almost the common decrescent dependence with respect to the Φ_{tot} (Fig. 8), which corresponds to the decrease in the PP yield stress with the inclusion content [Fig. 3(a)].

Fracture Topography

To examine damage processes responsible for the macroscopic fracture behavior of the composites found by the analysis of load-time diagrams, visual and microscopic observations of deformed specimens were carried out.

Macrophotographs of the impact-fractured specimens are given in Figure 11. Samples 1–3 are the ternary system specimens with Φ_{tot} = 27 vol %. Corresponding load-time curves are given in Figure 6. The fracture types of corresponding composites were classified as brittle on a macroscopic scale. The visual observation shows that stress whitening close to a notch tip preceded fracture of those specimens. In the MPP/GB/EPR composite, a stress-whitened zone is restricted to a most narrow zone just around a notch tip (sample 1). In the PP/GB/EPR composite, the stress-whitened zone is slightly larger. Nevertheless, it remains distinctly localized around the notch (sample 2). In the PP/GB/MEPR sample, the stress-whitened zone in the vicinity of the notch expands and becomes more diffuse. Moreover,

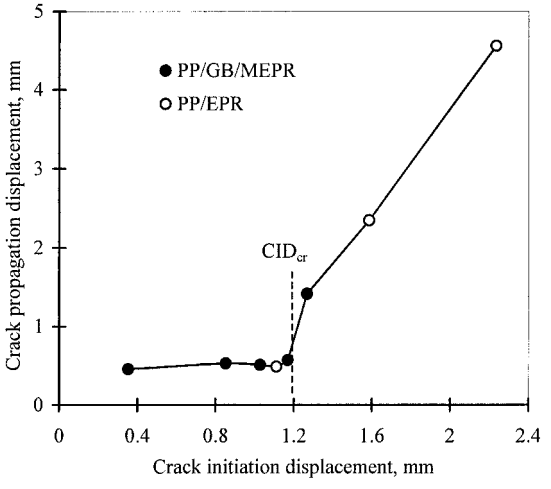

Figure 10 Relationship between crack initiation and crack propagation displacements for PP/GB/MEPR and PP/EPR systems.

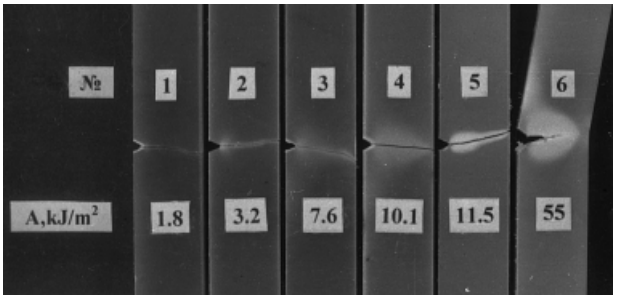

Figure 11 Macrophotographs of impact fractured specimens of MPP/GB/EPR (1), PP/GB/EPR (2), PP/GB/MEPR (3, 4), and PP/EPR (5, 6) composites. Total inclusion volume fraction in the ternary-phase systems: 27 (samples 1–3) and 53 (sample 4) vol %. The rubber volume fraction in the PP/EPR blends: 5 (sample 5) and 25 (sample 6) vol %.

stress-whitening extends over a specimen width (sample 3). An extent of a stress-whitened zone around the notch in a range of the MPP/GB/EPR–PP/GB/EPR–PP/GB/MEPR specimens correlates qualitatively well with an increase in the crack initiation displacements [Fig. 7(a)].

Figure 12(a–f) shows micrographs of nonetched impact fracture surfaces of specimens with Φ_{tot} = 27 vol %. Particle debonding and local matrix yielding around voids formed are observed for every three samples close to the notch tip [Fig. 12(a,c,e)]. Outside the notch region, the overall fracture surfaces look predominantly brittle, but fracture topographies of specimens show essential distinctions [Fig. 12(b,d,f)]. In the MPP/GB/EPR composite, a crack propagates through the PP phase as a result of a high PP–GB adhesion and failure is of a cohesive nature [Fig. 12(b)]. In the PP/GB/EPR composite, the GB particle debonding occurs throughout the fracture surface, resulting in an adhesive failure and certain shear lips are observed [Fig. 12(d)]. Debonding encapsulated particles is not seen on the fracture surface of the PP/GB/MEPR sample and failure is predominantly of a cohesive nature [Fig. 12(f)]. A noticeable increase in the matrix shear yielding takes place during fracture, resulting in the expansion of stress-whitening over this specimen width observed (Fig. 11, sample 3). Thus, the fracture morphology demonstrates the mixed-mode fracture for every three samples. The fractography data show that the macroscopic brittle fracture is in reality of a quasi-brittle nature. In this connection, the following comment should be made. A slightly extreme composition dependence of the fracture toughness for both MPP/GB/EPR and PP/GB/EPR composites [Fig. 9(c)] is a peculiar feature of quasi-brittle fracture.

A comparison of two macrophotographs of PP/GB/MEPR specimens (Fig. 11, samples 3 and 4) reveals that stress whitening expands from the restricted zone around the notch tip into a massive zone in the specimen bulk with increasing encapsulated GB content. In the specimen containing 53 vol % of encapsulated GB, the stress-whitened zone encompasses the entire cross-sectional area. Such fracture behavior of the ternary system with the core–shell inclusions is similar to that of the model PP/EPR system with increasing rubber content in the region of the brittle–ductile transition (Fig. 11, samples 5, 6). Ductile fracture of the PP/GB/MEPR specimen with Φ_{tot} = 53 vol % becomes apparent on the fracture surface as the pronounced matrix yielding and highly elongated voids close to the notch tip [Fig. 12(g)]. In a region away from the notch, the intense matrix shear yielding in the vicinity of encapsulated GB is evident, but particles remain attached to polymer and a cohesive failure takes place [Fig. 12(h)].

Deformation Mechanisms During Fracture

The Effect of Ternary Composite Morphology on the Plastic Flow Mechanism at Impact Loading

Deformation mechanisms accompanying the fracture were examined by SEM analysis of the structure of stress-whitened zone in a plane perpendicular to the fracture surface. Figure 13(a–c) shows SEM micrographs of the damage zone perpendicular to the crack plane for the quasi-brittle fractured specimens of ternary composites with Φ_{tot} = 27 vol %. The distinctive feature of the MPP/GB/EPR specimen characterized by high GB–PP adhesion is the multiple cracking of the PP matrix within the specimen bulk [Fig. 13(a)]. This kind of cracking indicates that the material fractured under plane strain or at least under mixed plane stress and plane strain conditions. In a side view of the PP/GB/EPR specimen with the phase-separate dispersion and weak GB-PP adhesion, the negligible amount of debonded GB particles and local matrix yielding around them are observed in the very narrow area close to the fracture plane [Fig. 13(b)]. In the PP/GB/MEPR sample, a plastic zone enlarges noticeably away from the fracture site [Fig. 13(c)]. Pronounced matrix yielding accompanied by the elastomer shell rupture and multiple voiding are responsible for the stress whitening in the vicinity of the notch observed in this specimen.

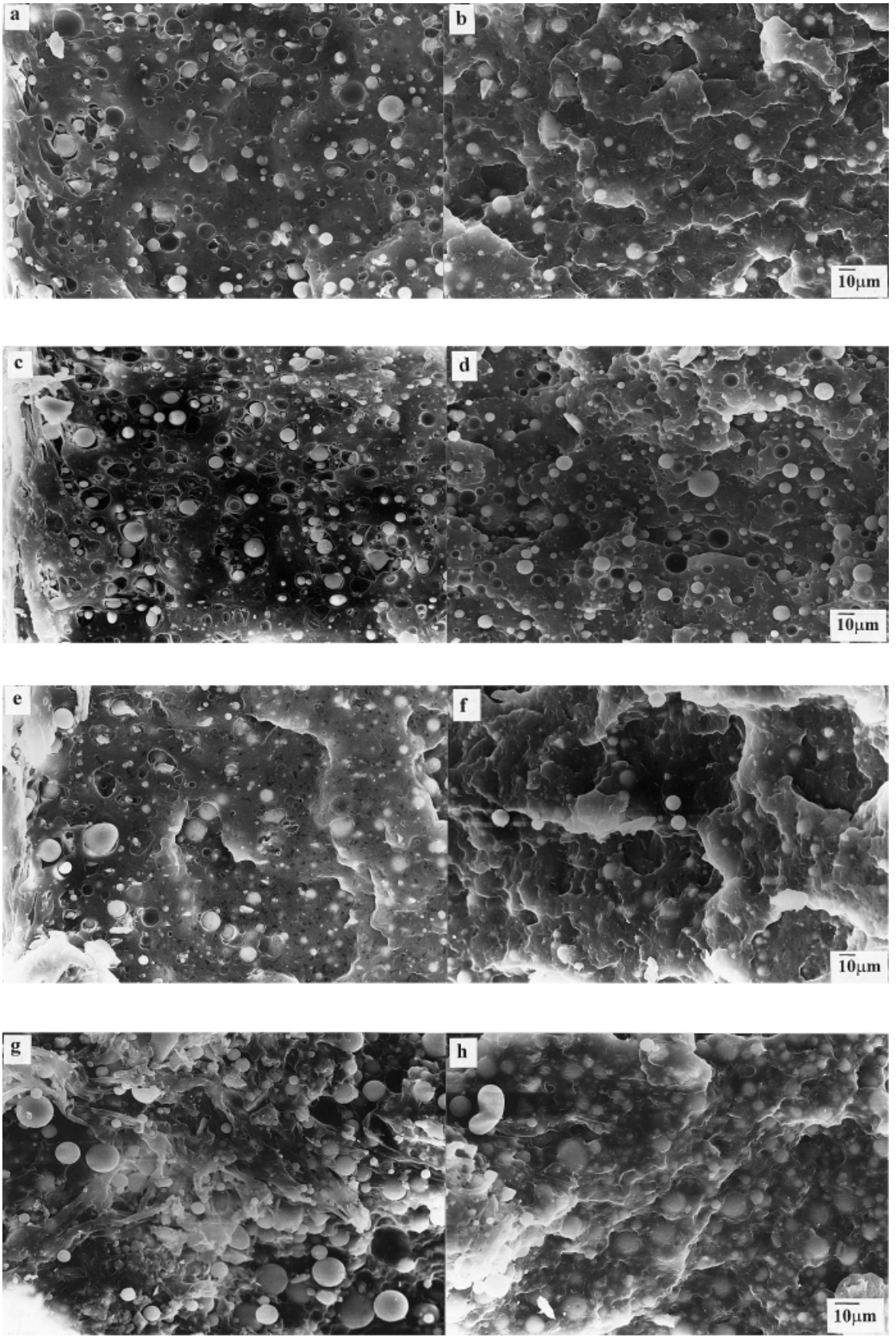

Figure 12 SEM micrographs of nonetched impact fracture surfaces for brittle fractured specimens with Φ_{tot} = 27 vol % (a–f) and tough fractured sample with Φ_{tot} = 53 vol % (g, h): MPP/GB/EPR (a, b), PP/GB/EPR (c, d), PP/GB/MEPR (e–h) systems. (a, c, e, g) The regions next to the notch tip; (b, d, t, h) away from the notch tip. The direction of crack propagation is from left to right.

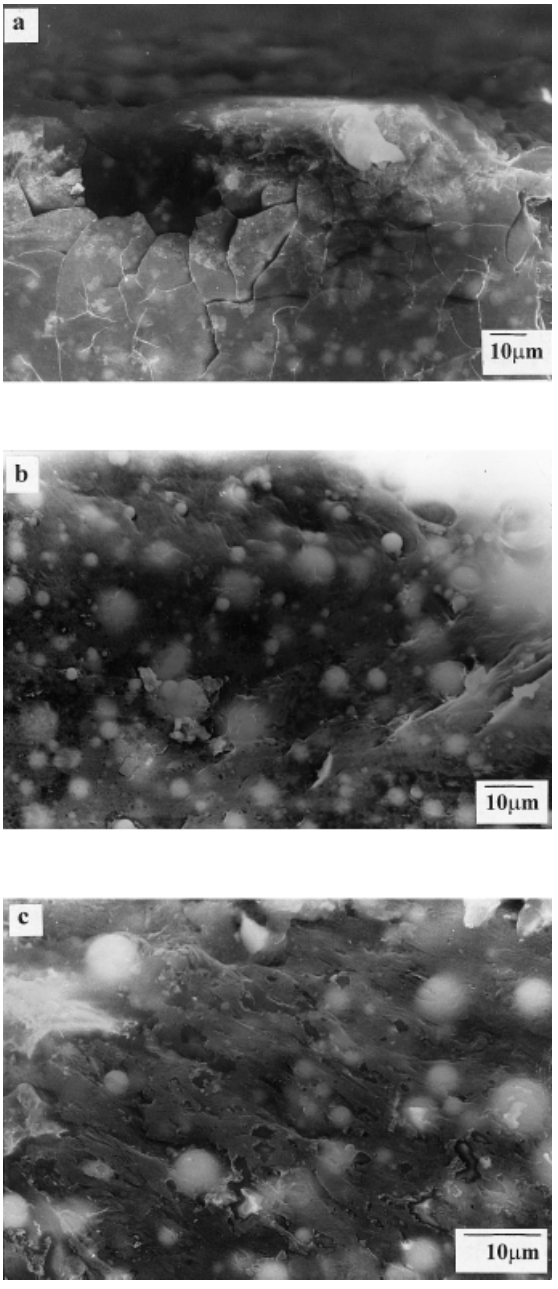

Figure 13 SEM micrographs of the damage zone perpendicular to the crack plane for the brittle fractured specimens of the ternary composites with Φ_{tot} = 27 vol %: MPP/GB/EPR (a), PP/GB/EPR (b), PP/GB/MEPR (c). The direction of crack propagation is from right to left.

The damage area of ductile-fractured PP/GB/MEPR specimen with Φ_{tot} = 53 vol % (impact strength, 10 kJ/m^2) is shown in Figure 14. Next to the fracture plane, a noticeable zone with highly deformed voids around GB particles as a result of intense matrix yielding is seen [Fig. 14(a)]. Below a yielded zone, the appreciable region is formed where crazelike deformation zones originate from encapsulated GB particles [Fig. 14(b)]. Figure 15 illustrates the damage area of tough fractured PP/EPR sample with 25 vol % of rubber. The expansion of the plastic zone over a large area far away from the fracture plane is responsible for the massive stress whitening and highest impact strength (55 kJ/m^2) of this sample.

The microscopic observation of both PP/GB/MEPR and PP/EPR composites shows that the transition from quasi-brittle to ductile fracture is accompanied by a change in the deformation mode from localized yielding near the fracture plane to macroscopic matrix yielding in the bulk. In this connection, it was supposed that the critical plastic deformation on an initiation stage, corresponding to a brittle-ductile transition (Fig. 10), comes from a critical precrack plastic zone necessary for the realization of a massive matrix yielding. This assumption agrees well with the

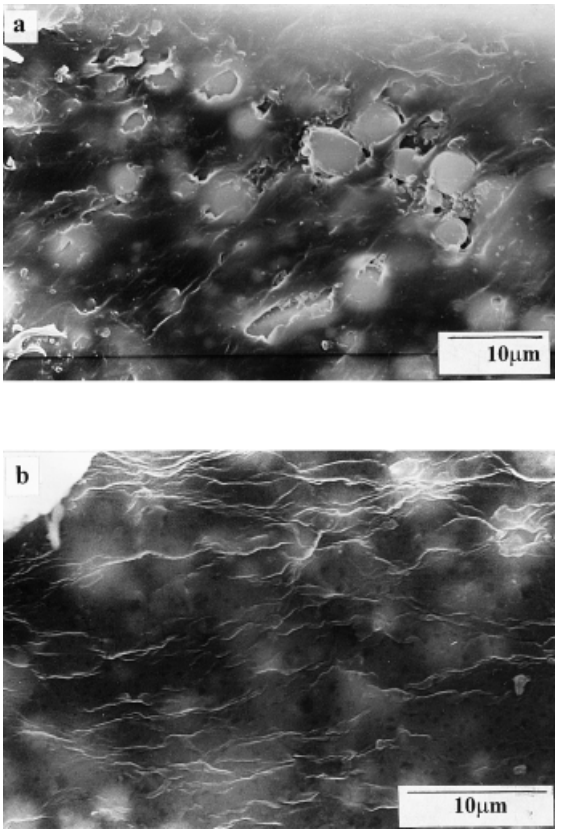

Figure 14 SEM micrographs of the damage zone perpendicular to crack plane for the tough fractured PP/GB/MEPR sample with Φ_{tot} = 53 vol % (A = 10 kJ/m^2): next to the fracture site (a) and in a region at a depth of $\approx$ 100 μm from the fracture site (b). The direction of crack propagation is from left to right.

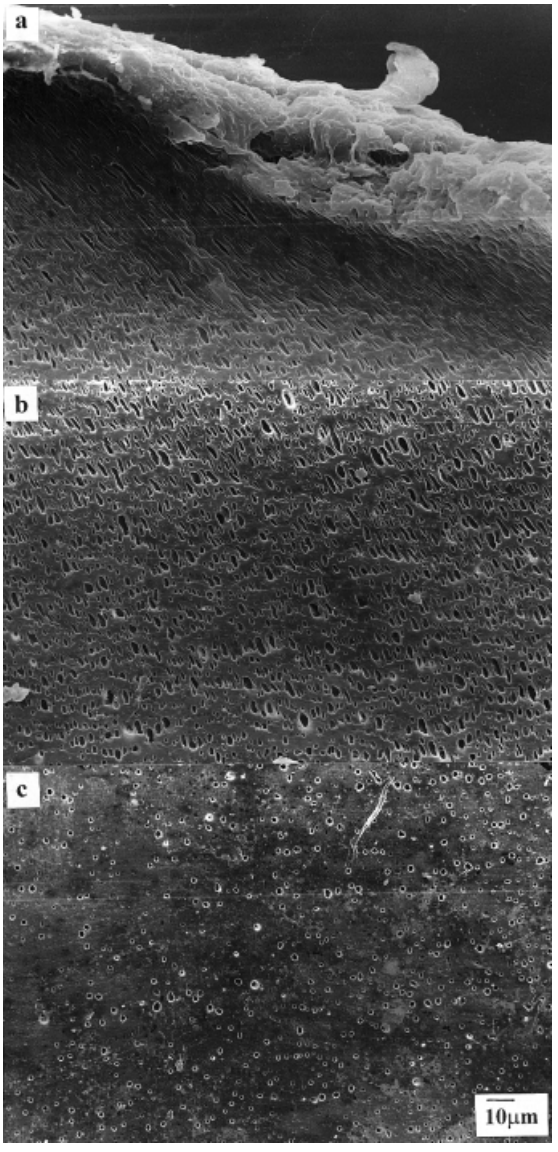

Figure 15 Typical damage zone perpendicular to crack plane for a tough fractured rubber-toughened PP specimen (Φ_{EPR} = 25 vol %, A = 55 kJ/m^2): next to the fracture site (a), in regions at depths of $\approx$ 500 μm (b), and $\approx$ 1000 μm (c) from the fracture site. The direction of crack propagation is from right to left.

criterion of the brittle–ductile transition based on the precrack plastic zone idea (or the critical displacement on an initiation stage) previously proposed for both the neat PC[22] and the rubber-modified PP and PA.[7,8]

The Energy Dissipation Micromechanisms at Ductile Fracture

The structure of a plastic zone at different distances from the fracture plane allows us to clarify microdeformation processes responsible for the massive matrix yielding followed by the ductile fracture. The typical damage zone for the model tough fractured PP/EPR specimen (Fig. 15) reflects a multistage energy dissipation mechanism. Profuse voiding within a large zone mostly remote from the fracture plane is evident that the rubber particle cavitation is an initial step of damage processes. Cavitational processes are followed by local matrix shear yielding in a vicinity of voids formed. Closer to the fracture site, the voids coalesce to form crazelike damage structures. The intense yielding of matrix ligaments between the created voids occurs within crazelike zones, resulting in highly deformed voids. In a region closest to the fracture plane, the crazed zones transform into a massive matrix yielding zone. The ductile fracture arises from the matrix ductile tearing during the crack propagation. The fixed energy dissipation microprocesses accompanying ductile fracture agree well with the rubber-toughening mechanism reported by numerous authors.[10,15,16,27,35–40] The main toughening mechanism in the rubber-modified polymers is based on the internal cavitation of rubber phase followed by voiding and dilatational yielding in the crazelike zones.

The fracture behavior of ternary-phase systems reveals that an ability to promote energy-dissipating processes depends on the inclusion nature, composite morphology, and interface adhesion. The SEM observation shows a series of possible voiding mechanisms (i.e., matrix crazing, rubber particle cavitation, filler particle–matrix debonding). Specific mechanisms are caused by modes of micromechanical processes at the inclusion–polymer interface on the early stage of the loading. In the case of phase-separate dispersion, voiding as a result of rigid particles debonding in the ternary systems with both a weak and high adhesion between GB and PP seem not to be an effective energy-dissipating channel. On the other hand, the encapsulation of rigid particles by an elastomer shell promotes a considerable raise in the effectiveness of the energy-dissipating processes during the fracture, including the intense matrix shear yielding around encapsulated GB particles and the formation of crazelike zones [Fig. 13(c) and 14]. Unfortunately, it is not clear which damage processes occur at the elastomer shell–polymer interface, but it is obvious from the SEM observation that the elastomer shell does not completely fail at the initial stage of loading. One could suppose a local rupture of elastomer

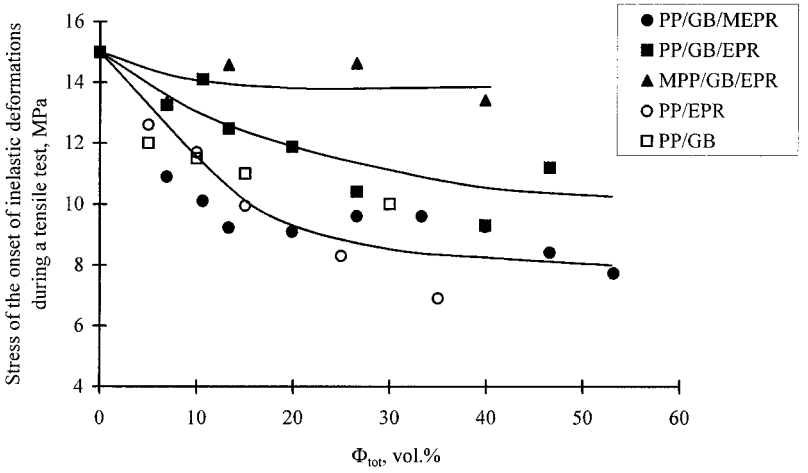

Figure 16 The effect of the composite morphology on the stress of the onset of inelastic deformation during a tensile test.

shell followed by microvoids generation in equatorial regions of the encapsulated GB particles takes place.

Correlation Between the Effectiveness of Energy-Dissipating Processes at Impact Loading and the Stress of the Onset of Inelastic Deformation at the Tensile Test

The multistage-toughening mechanism considered supposes that the most effective energy dissipation mechanism includes the widespread cavitational processes followed by shear yielding. Thus, the key role of inclusions in acting as impact modifiers is to induce these micromechanical-toughening mechanisms.

It was found for the rubber-modified polymers that the elastomer effectiveness depends on its ability to void nucleation. Namely, rising the toughening effect with a decrease in the stress at which the rubber particle cavitation starts was shown by Borggreve and coworkers[13,14] and also by Chiu and coworkers.[35] Because the start of the rubber cavitation is conformed to the onset of inelastic polymer deformation observed during a tensile test, the stress at which voiding in the polymer composites starts was evaluated from the stress of the onset of nonlinearity in the stress–strain curve.

Similarly, the stress at which voiding starts as a result of the rigid particle debonding in the particulate-filled polymers can be estimated.[41,42] From this viewpoint, we have analyzed an influence of the morphology of ternary-phase composites on the stress of the onset of nonlinearity in the σ-ε curve at the tensile test (Fig. 4). The stresses of the onset of inelastic deformations for the ternary composites as well as for both binary PP/GB and PP/EPR systems are plotted in Figure 16 as functions of Φ_{tot}. As seen from Figure 16, the stresses at which the inelastic deformation starts in MPP/GB/EPR composites with the high PP–GB adhesion are highest and close to that of the neat PP. The inelastic deformation in the PP/GB/EPR and PP/GB composites with a weak adhesion between PP and GB begins on an earlier stage of loading in comparison with those of the MPP/GB/EPR system. The lowest stresses of the onset of inelastic deformation are in the PP/GB/MEPR system and they are close to those of the rubber-modified PP. Thus, damage processes in the vicinity of both rubber and encapsulated GB particles start at the lower stress than the debonding stress at weak as well as at high polymer-filler adhesion. These data point to the strong dependence of the stress of the start of a local matrix yielding at the inclusion–polymer interface on the composite morphology, inclusion nature, and interfacial adhesion.

Comparison of Figures 16 and 3(b) shows also that the increase in the stress of the onset of the inelastic deformation is consistent with the decrease in the composites yield strain. It means that a tendency to the localization of plastic deformations during a tensile test in MPP/GB/EPR composites (Fig. 4) is caused by difficulty of the matrix shear yielding at the inclusion–polymer interface because of high adhesion.

A correlation between the stress at which the local matrix yielding starts at a tensile test and the impact behavior of the composites was found.

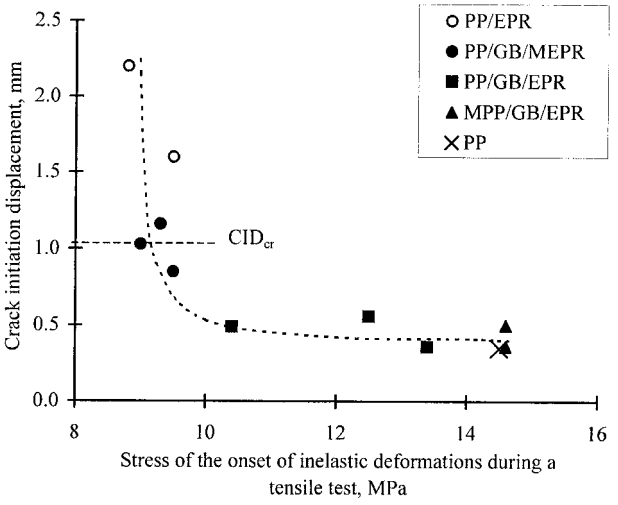

Figure 17 Correlation between the stress of the onset of inelastic deformation during a tensile test and the crack initiation displacement during impact test.

Figure 17 shows that the decrease in the stress at the onset of inelastic deformation in the σ-ε curve is consistent with an increase in a displacement on the crack initiation stage at the impact loading. It is seen that the achievement of the critical value of the CID is possible at the condition of the low stress of the local matrix yielding start. On the basis of these data, the effect of the ternary composite morphology on the energy-dissipating process effectiveness during crack initiation can be explained by the role of the stress at which voiding and sequent matrix shear yielding at the matrix-inclusion boundary start. So, at the same inclusion content, the density of crazelike zones formed in the material bulk before fracture will be higher in the system where the local matrix yielding is induced at the earlier stage. Further, high intensity of plastic deformation causes ductile fracture of ternary composites. Contrarily, in the case of restricted voiding owing to high debonding stress, only local particle debonding will occur close to the notch tip. Localized voiding will result in the low density of crazelike zones, followed by the quasi-brittle fracture. Thus, the transition to massive yielding in the presence of the GB coated by an elastomer shell is caused by a decrease in the stress of the matrix shear yielding at polymer–elastomer interface compared to the stress at which debonding of the original GB starts.

At the same time in both PP/GB/MEPR and PP/EPR systems, characterized by the same low stress of the local matrix yielding start, the crack initiation displacements increase gradually with an increase in inclusion volume fraction (Fig. 7). It means that a density of formed crazelike zones rises with the increase in the number of the local yielding nucleus. Also, the higher crack initiation displacement of the PP/EPR blend compared to ternary PP/GB/MEPR system at the same inclusion volume fraction can be explained by higher numbers of local yielding nucleus followed by higher density of formed crazelike zones. At the same inclusion volume fraction, the higher inclusion number in the binary PP/EPR blend compared to that of ternary system with encapsulated GB is apparently due to a larger GB particle size (1–10 μm) than that of rubber phase (0.5–2 μm). For these reasons, the critical plastic deformation on the initiation stage corresponding to the brittle-ductile transition is achieved under the higher volume fraction of the encapsulated GB particles.

CONCLUSION

The following three types of the phase morphology of ternary PP/GB/EPR composites were prepared: (1) separate dispersion of phases and low GB-PP adhesion; (2) separate dispersion of phases and high GB–PP adhesion, using MPP; and (3) encapsulation of GB by an elastomer shell, using MEPR. A rigid filler content was varied in the range of 5–40 vol % at a fixed volume fraction ratio EPR/GB equal to 0.33. The deformation and fracture behavior of ternary-phase composites as well as of model binary systems containing either rubbery (PP/EPR) or rigid (PP/GB) inclusions was investigated.

The Young's moduli of ternary-phase composites are located in the bounds corresponding to binary composites containing either rigid or soft inclusions. The modulus of ternary systems containing separately dispersed rubber particles increases with an increase in the total inclusion volume fraction and does not depend on matrix–filler interfacial adhesion. When rubber forms a soft interlayer on the rigid particle surface, modulus values of ternary-phase composites were found to remain close to that of PP at every Φ_{tot} (i.e., a reduction of reinforcing efficiency of the filler takes place).

Notched impact strength of composites was measured by Izod and three-point bending tests. It was shown that a manner of the rubber-phase disposition strongly affects fracture behavior of the ternary-phase composites. When the EPR and

GB particles are distributed separately in PP matrix, the impact strength of ternary systems is slightly higher than that of binary PP/GB composites, at that increasing interfacial adhesion between GB and PP matrix results in the composite toughness decreasing. In contrast, the encapsulation of rigid particles by elastomer shell essentially improves the composite impact strength.

The fracture types of composites were determined by an analysis of three-point bending load-time diagrams and SEM observations of specimen impact fracture surfaces and the structure of damage zones perpendicular to the crack plane. The ternary systems with a separate dispersion of components with both weak and high adhesion exhibited a quasi-brittle fracture. In contrast, the formation of a soft interlayer on a rigid particle surface resulted in an expansion of stress-whitened plastic zone far away from the fracture site. With increasing encapsulated GB particles, a brittle–ductile transition occurred similar to the rubber-modified PP. The typical rubber-toughening mechanism included the internal cavitation of rubber phase followed by voiding and dilatational yielding in the crazelike zones. In the ternary-phase system containing core–shell inclusions, the main modes of energy-dissipating micromechanisms were found to be a generation of crazelike zones in the vicinity of encapsulated GB particles and a massive matrix yielding accompanied by an elastomer shell rupture close to the fracture plane.

The toughening of both PP/GB/MEPR and PP/GB systems with inclusion fraction increasing was preceded by an increase in a plastic deformation on a crack-initiation stage. Load–time curves analysis revealed that accumulation of a critical plastic deformation on a crack initiation stage (corresponding to critical precrack plastic zone necessary for a realization of the massive matrix yielding) is a criterion of brittle–ductile transition in those two systems.

The dominating role of the stress of onset of local failure microprocesses at the inclusion–matrix boundary in energy-dissipating mechanisms was shown. The lower stress at which a local matrix yielding starts at elastomer shell–PP interface compared to the stress of debonding original GB was responsible for increasing energy adsorbed during initiation stage in the system with encapsulated GB. Thus, the encapsulation of rigid particles by elastomer shell, from the viewpoint of the effect on the composite fracture toughness, is equal to the increase in the effective concentration of the rubber particles.

The optimal stiffness–toughness balance was attained as a result of coating the rigid particles by elastomer shell.

The authors thank the Russian Foundation of Fundamental Research, Project No. 01-03-32043, for financial support of this work.

REFERENCES

1. Orazio, L. D.; Mancarella, C.; Martuscelli, E.; Polato, F. Polymer 1991, 32, 1186.
2. Karger-Kocsis, J.; Kallo, A.; Kuleznev, V. N. Polymer 1984, 25, 279.
3. Wu, S. Polymer 1985, 26, 1855.
4. Wu, S. J Appl Polym Sci 1988, 35, 549.
5. Bartczak, Z.; Argon, A. S.; Cohen, R. E.; Weinberg, M. Polymer 1999, 40, 2331.
6. Van der Wal, A.; Mulder, J. J.; Oderkerk, J.; Gaymans, R. J. Polymer 1998, 39, 6781.
7. Van der Wal, A.; Nijhof, R.; Gaymans, R. J. Polymer 1999, 40, 6031.
8. Dijkstra, K.; Ter Laak, J.; Gaymans, R. J. Polymer 1994, 35, 315.
9. Van der Wal, A.; Verheul, A. J. J.; Gaymans, R. J. Polymer 1999, 40, 6057.
10. Van der Wal, A.; Gaymans, R. J. Polymer 1999, 40, 6067.
11. Inoue, T.; Suzuki, T. J Appl Polym Sci 1995, 56, 1113.
12. Ishikawa, M.; Sugimoto, M.; Inoue, T. J Appl Polym Sci 1996, 62, 1495.
13. Borggreve, R. J. M.; Gaymans, R. J.; Schuijer. J. Polymer 1989, 30, 71.
14. Borggreve, R. J. M.; Gaymans, R. J.; Eichenwald, H. M. Polymer 1989, 30, 78.
15. Lazzeri, A. L.; Bucknall, C. B. J Mater Sci 1993, 28, 6799.
16. Lazzeri, A. L.; Bucknall, C. B. Polymer 1995, 36, 2895.
17. Ishikawa, M.; Takahasi, H. J Mater Sci 1991, 26, 1295.
18. Ishikawa, M.; Ushui, K. Polymer 1996, 37, 1601.
19. Ishikawa, M.; Ushui, K.; Kondo, Y. Polymer 1996, 37, 5375.
20. Muratoglu, O. K.; Argon, A. S.; Cohen, R. E.; Weinberg, M. Polymer 1995, 36, 4771.
21. Muratoglu, O. K.; Argon, A. S.; Cohen, R. E.; Weinberg, M. Polymer 1995, 36, 4787.
22. Chang, F.-C.; Hsu, H.-C. J Appl Polym Sci 1991, 43, 1025.
23. Jancar, J.; Dibenedetto, A. T. J Mater Sci 1994, 29, 4651.
24. Jancar, J.; Dibenedetto, A. T. J Mater Sci 1995, 30, 1601.
25. Jancar, J.; Dibenedetto, A. T. J Mater Sci 1995, 30, 2438.

26. Stricker, F.; Multhaupt, R. J Appl Polym Sci 1996, 62, 1799.
27. Mouzakis, D. E.; Stricker, F.; Multhaupt, R.; Karger-Kocsis, J. J Mater Sci 1998, 33, 2551.
28. Hornsby, P. R.; Premphet, K. J Mater Sci 1997, 32, 4767.
29. Hornsby, P. R.; Premphet, K. J Appl Polym Sci 1998, 70, 587.
30. Premphet, K.; Horanont, P. J Appl Polym Sci 2000, 76, 1929.
31. Molnar, Sz.; Pukanzky, B.; Hammer, C. O.; Maurer, F. H. J. Polymer 2000, 41, 1529.
32. Dubnikova, I. L.; Berezina, S. M.; Oshmyan, V. G. Polymers 2000, Proceedings of the Conference Devoted to the 40th Anniversary of the Polymers and Composites Department of Semenov Institute of Chem Physics, RAS, Moscow, 2000; Vol. 2, p 234.
33. Van der Wal, A.; Mulder, J. J.; Thijs, H. A.; Gaymans, R. J. Polymer 1998, 39, 5467.
34. Van der Wal, A.; Mulder, J. J.; Gaymans, R. J. Polymer 1998, 39, 5477.
35. Chiu, C. J.; Vijayan, K.; Kirby, D.; Hiltner, A.; Baer, E. J Mater Sci 1988, 23, 2521.
36. Michler, G. H. Acta Polymer 1993, 44, 113.
37. Kim, G.-M.; Michler, G. H.; Gahleitner, M.; Fiebig, J. J Appl Polym Sci 1996, 60, 1391.
38. Michler, G. H. J Macromol Sci 1999, B38, 787.
39. Kausch, H.-H.; Gensler, R.; Grein, C. J Macromol Sci 1999, B38, 803.
40. Gensler, R.; Plummer, C. J. G.; Grein, C.; Kausch, H.-H. Polymer 2000, 41, 3809.
41. Dubnikova, I. L.; Oshmian, V. G.; Gorenberg, A. Ya. J Mater Sci 1997, 32, 1613.
42. Dubnikova, I. L.; Muravin, D. K.; Oshmyan, V. G. Polym Eng Sci 1997, 37, 1301.